A first approximation to the modeling of vapor plume evolution in laser welding

M. Raja Kumar, I.Tomashchuk*, J.-M. Jouvard, M. Duband
Laboratoire Interdisciplinaire Carnot de Bourgogne, UMR CNRS 6303 - Université de Bourgogne – Franche Comté, 12 rue de la Fonderie – 71200 Le Creusot, France
* iryna.tomashchuk@u-bourgogne.fr

Abstract : A quantification of spatial and temporal evolution of laser-induced plume would enhance the comprehension of results from high speed imaging and optimization of emission spectroscopy acquisition parameters. What temperature and concentrations of the evaporating species are sufficient for obtaining an emission spectrum? Which part of the plume should be targeted? How long does the plume persist after the extinction of the laser? To answer these questions, a first approximation to the multiphysical modeling of the vapor plume during a millisecond scale Yb:YAG laser pulse on the metallic material was attempted. A time-dependent 2D axisymmetric model comprising strongly coupled heat transfer, fluid flow, diffusion and moving mesh problems is proposed. In the metal domain, the heat transfer involving the evaporative energy loss is coupled with a non-isothermal flow represented by incompressible Navier-Stokes equation, which takes into account recoil pressure, surface tension, Marangoni effect and gravity. In the gas domain, the non-isothermal flow represented by compressible Navier-Stokes equation is strongly coupled with diffusion equation, which is based on the flux of evaporating metal atoms and Fuller approximation of diffusion coefficient. The proposed model was applied to the case of aluminum and compared with the experimental results of high-speed imaging and post-mortem analysis of the impact zone.

Keywords: laser welding, vapor plume, multiphysics.

1. Introduction

The analysis of vapor plume produced during a high power laser-metal interaction allows better comprehension of keyhole dynamics and can give a hint about the characteristics of metallic vapor inside the keyhole. The main methods of plume analysis nowadays are high speed imaging [1], Schlieren imaging [2] and emissive spectroscopy [3]. The use of high-speed imaging in combination with different VIS and IR filters allows obtaining the bright image of the plume induced mainly by the continuous emission of the hot vapor on a chosen wavelength, while Schlieren imaging represents the existing gradient of density. The emissive spectroscopy of laser-induced plume allows identifying the species that form the vapor, estimating the vapor temperature through Boltzmann plot method etc [3]. However, there is no experimental method capable to capture a velocity field inside the plume that should not be confused with the propagation velocity of plume envelope, which can be easily calculated using above-mentioned imagining techniques. Moreover, the concentration of evaporated species and their dilution in the ambient gas is quite complicated to evaluate experimentally.

The emission spectroscopy analysis of "classical" (not nano or pico-second) laser welding of aluminum met with many difficulties [4]: the absence of emission lines besides the fundamental transitions at 394.4 and 396.1 nm, low intensity of the continuous emission and the fluctuations of the signal. The numerical modeling of the laser-induced plume would provide the necessary information about the influence of welding parameters on the plume temperature and the concentration of the evaporating species, to identify the energy densities sufficient for the acquisition of a good quality emission spectrum. Moreover, the comprehension of species dilution in the plume would help with would help with optimization of signal acquisition parameters from the different parts of the plume. The information about the extinction of the plume at the end of interaction would also be helpful in the interpretation of time-dependent spectra intensity.

The recent progress around the numerical modeling of laser–induced vapor jets was closely related with the need to comprehend the loss of metallic powder in SLM and LMD techniques. The first COMSOL Multiphysics model of laser-induced vapor jet was proposed by Eppes et al [5] and was based on the fixed mesh and phase transitions created by temperature-dependent properties. The further works on the plume propagation with COMSOL Multiphysics were based on two concurrent methods: level set [6] and ALE [7]. The level set method allows taking into account the complex fluctuations of metal/gas interface, like the formation of spatter or volume defects in the melted zone. However, it implies the solving of the common incompressible Navier-Stokes equation for both metal and gas domains. ALE method does not model the discontinuities of metal/gas interface, but it allows separating the incompressible fluid flow in the metal domain from the vapor expansion problem in gas domain, where compressible flow is necessary for the realistic representation of plume behavior. Mayi et al. [7] described such ALE-based numerical scheme that involves two separate Navier-Stokes equations coupled with heat transfer, where the propagation of metal atoms in the plume was evaluated using the atomic fraction as the solved variable in Fick equation. The resulting plume had a mushroom structure with a characteristic Rayleigh-Taylor instability, and the maximal gas velocity next to the metal/gas interface exceeded 100 m/s. In view of typical velocities of the vapor jet and the formation of lateral vortexes, the laminar flow formulation represents a first approximation to the description of plume behavior. The existing turbulence-based models deal only with vapor domain, without considering the free surface deformation. Arshed et al [8] proposed a k-ε turbulence model for the description of laser-induced jet that showed a good correspondence between calculated and experimental heights of the plume. Bidare at al. [2] described the plume behavior using RANS SST turbulence model in COMSOL Multiphysics.

The present study is dedicated to the multiphysical modeling of the vapor plume evolution during a millisecond Yb:YAG laser pulse on the metal surface. The proposed 2D axisymmetric time-dependent model uses the deformed geometry approach for the description of metal/gas interface and solves separate Navier-Stokes equations for metal and gas domains, strongly coupled with the respective heat transfer equations. As the turbulence effects were not taken into

account, the proposed model represents a first approximation to the auto-consistent description of the plume. The main novelty of this work is the calculation of molar concentration of metal atoms in the plume using Fuller approximation of diffusion coefficient of metal atoms in the ambient atmosphere. The proposed model was applied to the case of aluminum and compared with experimental results of high speed imaging and post-mortem analysis of the impact zone.

2. Governing equations

The complete description of plume propagation during the laser impact demands the coupled solving of heat transfer, fluid flow and mass transfer problems in the gas phase, which comprises both air and evaporating metal atoms. As the evaporation process occurring in the melted zone acts as the motor of plume formation, the heat transfer and fluid flow problems should be accurately solved for the metal domain as well. Consequently, the problem of plume propagation is strongly multiphysical and needs several couplings between the different kinds of physics. The scheme of the proposed multiphysical couplings is provided on the Figure 1. A strong coupling is established between heat transfer and fluid flow in the metal, to provide the temperature of melted zone surface. The output vaporization flux controls the temperature of metal/gas interface, necessary for resolving the thermal field in the gas domain. The second strong coupling is established between heat transfer, fluid flow and the diffusive transport of metal atoms in the air, as the local physical properties must depend on the fraction of metal atoms in the plume. The position of free surface between gas domain and metal domain is calculated based on the velocity fields of both liquid metal and plume jet. The governing equations and main boundary conditions for each physics are described in the following sub-chapters. For the reduction of calculation time, a 2D axisymmetric formulation was used.

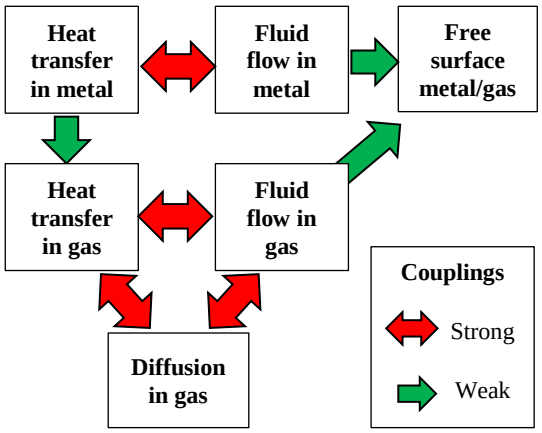

Figure 1. The scheme of multiphysical couplings.

2.1. Heat transfer in the metal

Heat transfer equation for the metal was solved in time-dependent form

$$\rho_m \, C_{p\ m}^{eq} \frac{\partial T_m}{\partial t} + \rho_m \, C_{p\ m}^{eq} \overrightarrow{U_m} \cdot \overrightarrow{\nabla} T_m = \overrightarrow{\nabla} \cdot \left(k_m \overrightarrow{\nabla} T_m \right) \quad (1)$$

with ρ_m - density of metal (kg/m^3), $C_{p\ m}^{eq}$ – equivalent heat capacity of the metal (J/(kg·K)), k_m – thermal conductivity of the metal (W/(m·K)), T_m – solved metal temperature (K) and t – time (s).

The energy supply from a standalone laser pulse was introduced as surface Gaussian heat source applied to metal/gas interface:

$$q_m^{laser} = \frac{2\,a\,P_l}{\pi\,{R_l}^2} exp^{-2\frac{r^2}{{R_l}^2}} \cdot \left(t \geq t_{imp} \right) \quad (2)$$

with a – absorption coefficient of laser radiation, P_l – laser power (W), R_l – laser spot radius (m) and t_{imp} – the duration of laser pulse (ms).

The heat loss through evaporation was represented by surface vaporization heat flux applied to metal/gas interface [9]:

$$q_m^{vap} = -(1-\beta_r) L_m^{vap} \sqrt{\frac{M_m}{2\pi R T_m}} P_{sat} \quad (3)$$

where β_r – the recombination coefficient, L_m^{vap} – latent heat of vaporization (J/kg), M_m – molar mass of the metal (kg/mol), R – ideal gas constant (J/(mol·K)) and P_{sat} – pressure of saturated metal vapor (Pa).

For the lateral walls of the metal domain, an ambient temperature was applied.

2.2. Fluid flow in the metal

The metal domain was considered as an incompressible Newtonian liquid having T-dependent dynamic viscosity μ_m (Pa·s). The time-dependent laminar flow is governed by Navier-Stokes equation:

$$\rho_m \frac{\partial \overrightarrow{U_m}}{\partial t} + \rho_m \left(\overrightarrow{U_m} \cdot \overrightarrow{\nabla} \right) \overrightarrow{U_m} = \overrightarrow{\nabla} \cdot \left\{ p_m 2[I] + \mu_m \left[\nabla \overrightarrow{U_m} + \right. \right.$$
$$\left. \left. + \left(\nabla \overrightarrow{U_m} \right)^T \right] \right\} + \vec{F}_D + \rho_m \vec{g}$$
$$\rho_m \overrightarrow{\nabla} \cdot \overrightarrow{U_m} = 0 \quad (4)$$

where p_m is the relative pressure (Pa) and $\overrightarrow{U_m}$ is the velocity field in the metal domain

$$\overrightarrow{U_m} = \begin{cases} u_m \\ w_m \end{cases} \quad (5)$$

To inhibit the convection in the solid part of the domain, Darcy damping force was applied [10]:

$$\vec{F}_D = K_{ip} \overrightarrow{U_m} \quad (6)$$

where K_{ip} is an isotropic permeability defined as:

$$K_{ip} = \frac{-C(1-f_l)^2}{(f_l^3 + b)} \quad (7)$$

with constants $C = 1 \cdot 10^6$, $b = 1 \cdot 10^{-3}$ and f_l - numerical fraction of liquid that turns to 1 when the temperature becomes equal to the melting point T_f (K) :

$$f_l = flc2hs\left(T_m - (T_f - dT), dT \right) \quad (8)$$

At the metal/gas interface, the recoil pressure [11] was applied:

$$P_r = \left(\frac{1+\beta_r}{2} \right) P_{sat} \quad (9)$$

where the pressure of saturated vapor is given as :

$$P_{sat} = P_0 exp^{\left[\frac{L_m^{vap} M_m}{R} \left(\frac{1}{T_m^{vap}} - \frac{1}{T_m} \right) \right]} \quad (10)$$

The surface tension σ (N/m) was given as :

$$\sigma = \sigma_f + \gamma_m T_m \quad (11)$$

where σ_f (N/m) is the surface tension at fusion temperature and γ_m is a temperature coefficient of surface tension (N/(m·K)).

Surface tension is taken into consideration through Laplace equation [12] :

$$p_m \cdot \vec{n} = -\sigma \frac{\partial \vec{t}}{\partial s} \quad (12)$$

where $\vec{t}$ is the tangent vector to the free surface s.

Finally, a thermocapilary convection is taken into account:

$$\left\{-p_m[I] + \mu_m \left[\nabla \overrightarrow{U_m} + \left(\nabla \overrightarrow{U_m}\right)^T\right]\right\} \vec{n} = \gamma_m \overrightarrow{\nabla_t} T_m \quad (13)$$

Non-slip condition is applied to the lateral and bottom boundaries.

2.3. Material properties of in the metal domain

The physical properties of the metal are introduced as Heaviside functions of temperature, with T-dependent expressions for solid (A_m^s) and liquid (A_m^l) state:

$$A_m = A_m^s + (A_m^l - A_m^s)\, f_l, \quad (14)$$

where $A_m = a, \rho_m, C_{p\ m}^{eq}, k_m, \mu_m, \sigma, \gamma_m$.

The latent heat of fusion of L_m^f (J/kg) is taken into account by means of equivalent enthalpy approach [13]:

$$C_{p\ m}^{eq} = C_{p\ m}^{s} + \left(C_{p\ m}^{l} - C_{p\ m}^{s}\right) f_l + + L_m^f \frac{exp\ \frac{-\left(T-T_f\right)^2}{dT^2}}{\sqrt{\pi\, dT^2}}. \quad (15)$$

2.4. Heat transfer in the gas phase

Heat transfer equation for the gas phase is solved in time-dependent form:

$$\rho_g\, C_{p_g} \frac{\partial T_g}{\partial t} + \rho_g\, C_{p_g} \overrightarrow{U_g} \cdot \overrightarrow{\nabla} T_g = \overrightarrow{\nabla} \cdot \left(k_g \overrightarrow{\nabla} T_g\right) \quad (16)$$

with ρ_g - density of gas phase (kg/m^3) given by the ideal gas law (equation 25) , C_{p_g} – equivalent heat capacity of the gas at constant pressure (J/(kg·K)), k_g – thermal conductivity of the gas (W/(m·K)), T_g – solved temperature of the gas (K) and t – time (s).

The general inward heat flux at metal/gas interface is given as:

$$q_g^{vap} = -q_m^{vap} \quad (17)$$

Outflow condition is applied to the top and lateral boundaries.

2.5. Fluid flow in the gas phase

In the gas domain, a compressible laminar flow is described by Navier-Stokes equation in time-dependent form:

$$\rho_g \frac{\partial \overrightarrow{U_g}}{\partial t} + \rho_g \left(\overrightarrow{U_g} \cdot \overrightarrow{\nabla}\right) \overrightarrow{U_g} = \overrightarrow{\nabla} \cdot \{p_g 2[I] + [K]\} + \rho_g \vec{g}$$

$$\frac{\partial \rho_g}{\partial t} + \overrightarrow{\nabla} \cdot \left(\rho_g \overrightarrow{U_g}\right) = 0$$

$$[K] = \mu_g \left[\nabla \overrightarrow{U_g} + \left(\nabla \overrightarrow{U_g}\right)^T\right] - \frac{2}{3} \mu_g \left(\vec{\nabla} \cdot \overrightarrow{U_g}\right)[I] \quad (18)$$

where μ_g is the dynamic viscosity of the gas phase and $\overrightarrow{U_g}$ is the velocity field in the gas domain:

$$\overrightarrow{U_g} = \begin{cases} u_g \\ w_g \end{cases} \quad (19)$$

The recoil pressure is applied on the metal/gas interface:

$$P_r = \left(\frac{1+\beta}{2}\right) P_{sat} \quad (20)$$

Open boundary condition with zero viscous stress is applied to top and lateral boundaries.

2.6. Diffusion problem in the plume

For calculating the concentration field of metal atoms c_m (mol/m^3) during the evaporation process, Fick equation is solved in the gas domain

$$\frac{\partial c_m}{\partial t} + \overrightarrow{\nabla} \cdot \overrightarrow{J_m} + \overrightarrow{U_g} \cdot \overrightarrow{\nabla} c_m = 0$$

$$\overrightarrow{J_m} = -D_m \overrightarrow{\nabla} c_m \quad (21)$$

where the diffusion coefficient of metal atom in the gas phase D_m (m²/s) is estimated using Fuller approximation of Chapman-Enskog equation [14]:

$$D_m = \frac{1 \cdot 10^{-3} T_g^{1.75} \cdot \left(\frac{1}{M_m} + \frac{1}{M_{air}}\right)^{0.5}}{p_g \left[\left(\sum V_m\right)^{1/3} + \left(\sum V_{air}\right)^{1/3}\right]^2} \quad (22)$$

where M_m and M_{air} are the molar mass of metal and air respectively (g/mol), p_g – absolute gas pressure (atm), $\sum V_m$ and $\sum V_{air}$ are the diffusion volumes of metal atom and air.

The general inward flux of metal atoms is applied to the metal/gas interface:

$$\overrightarrow{J_v} = \frac{(1-\beta_r)\sqrt{\frac{M_m}{2\pi R T_m}} P_{sat}}{M_m} \vec{n} \quad (23)$$

The outflow condition is applied to the top and lateral boundaries.

The solved molar concentration of the metal allows to express the local molar fraction of metal atoms in the gas phase φ_m as follows:

$$\varphi_m = c_m \frac{R T_g}{p_g} \quad (24)$$

2.7. Material properties of the gas domain

The gas phase is represented as a mixture between the air and the metal atoms. The density of this mixture is given by ideal gas law

$$\rho_g = \frac{PM}{R T_g} \quad (25)$$

where M is the molar mass of the mixture that depends on local fraction of metal atoms:

$$M = M_m \varphi_m + M_{air}(1 - \varphi_m) \quad (26)$$

All other properties of gas phase ($A_g = C_{p_g}, k_g, \mu_g$) are also represented as functions of local fraction of metal atoms:

$$A_g = A_g^m \varphi_m + A_g^{air}(1 - \varphi_m) \quad (27)$$

2.8. Moving mesh

The displacement of metal/gas interface is given by the normal velocity $\overrightarrow{V_n}$ formulated as:

$$\overrightarrow{V_n} = f_l\left(\overrightarrow{V_l} + \overrightarrow{V_g}\right) \quad (28)$$

where $\overrightarrow{V_l}$ is the superposition of the velocity fields of the melted metal and the gas given as

$$\overrightarrow{V_l} = \frac{\rho_m\left(u_m \overrightarrow{n_r} + w_m \overrightarrow{n_z}\right) - \rho_g\left(u_g \overrightarrow{n_r} + w_g \overrightarrow{n_z}\right)}{\rho_m - \rho_g} \quad (29)$$

and $\overrightarrow{V_g}$ is the velocity of the vaporization front

$$\overrightarrow{V_g} = \frac{(1-\beta_r)\sqrt{\frac{M_m}{2\pi R T_m}} P_{sat}}{\rho_m} \vec{n} \quad (30)$$

3. Use of COMSOL Multiphysics® Software

The model is created in a 2D axi-symmetric form and comprises a rectangular metal domain of 1x2.5 mm² and a gas domain of 11x2.5 mm² (Figure 2). The rectangular mesh of 0.06

mm is applied to both domains. Additionally, a 0.01 mm mesh size is applied to the metal/gas interface and a 0.03 mm mesh size - to the external boundaries and symmetry axis.

Two separate modules of heat transfer in fluids are used : Metal Heat Transfer (calculated variable T_m) and Gas Heat Transfer (calculated variable T_g). Laminar flow with incompressible formulation is solved for the metal domain (calculated variables $\overrightarrow{U_m}$ and p_m), with surface tension and thermocapillary effects programmed in a weak form. Compressible Laminar flow is solved for the gas domain (calculated variables $\overrightarrow{U_g}$ and p_g). The Non-Isothermal flow Multiphysics is used for sharing the density of the gas phase defined in the Gas Heat Transfer module with Compressible Laminar flow module. The transport of evaporating metal atoms is calculated with Transport of Diluted Species module. In order to account for the loss of matter through evaporation, the *Deformed Geometry* module with Yeoh smoothing was used to describe the motion of metal/gas interface. The progressive stiffening of the meshes (S) in function of local vertical displacement (*material.dZ*) was introduced in order to lower the risk of excessive mesh deformation and inversion:

$$S = s_{const}\, flc2hs(abs(material.dZ)\text{-}2e\text{-}5,\ 1e\text{-}5) \quad (31)$$

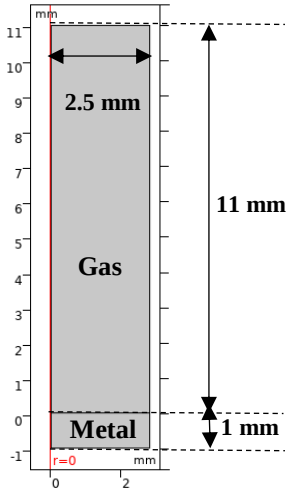

Figure 2. Model geometry.

Due to the high complexity of this multiphysical model, the intricacies are managed by profuse application of consistent and inconsistent numerical stabilization coefficients. However, the influence of inconsistent stabilization on the quality of obtained solution has been verified.

The calculation was performed over the time (4 ms) twice superior to the pulse duration (2 ms), to include the process of plume extinction and melt solidification. A time step of 1 µs was applied for better convergence. The user controlled relative tolerance was fixed to 0.05. A time-dependent solver MUMPS using full coupling with Automatic Highly nonlinear Newton method was used. The model was solved on the workstation with Intel ® Xeon ® CPU E5-2699v4 (2 processors, 2.2 GHz, 44 cores) and 256 Gb RAM. The longest calculation took ~ 5 h.

4. Experiment

The experiments were performed using a Yb:YAG laser (λ =1030 nm) TruDisk 6001 (Trumpf) at a focal distance of 200 mm, focused spot diameter of 0.6 mm and pulse duration of 2 ms. Laser beam of 3 kW power was focused at the top surface of A5754 aluminum alloy plate. No gas protection of the melted zone was used. The dimensions of the melted zone were evaluated post-mortem using a scanning electronic microscope JSM-6610LA (Jeol), equipped with an EDS analyzer.

The plume development was observed with a high speed camera Phantom V9.1 using 810 nm filter that allows highlighting the zones with continuous thermal emission. The resolution of the image was of 480x480 px, which corresponded to the dimension of the filmed zone of about 15x15 mm². Framerate of 6420 pps and exposure time of 120 µs were used.

5. Results and discussion

5.1. Validation of the model

In the first place, the laser impact on the surface of A5754 plate after a 2 ms long pulse was compared with the calculated melted zone (Figure 3). The measured radius of the impact (480 µm) was close to the calculated radius (410 µm). A ~15 % relative error can be explained by a large numerical mushy zone necessary for the optimal numerical convergence of the model. The irregular ejection of metal droplets out of the impact zone was not reflected by the model.

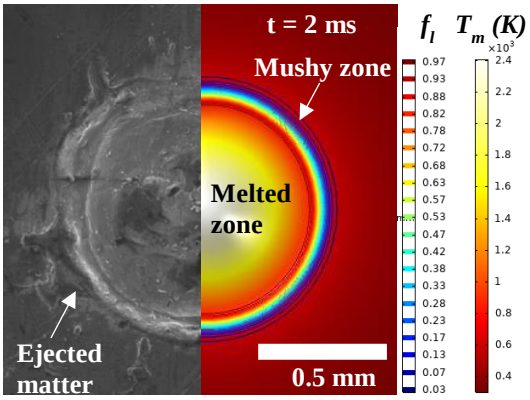

Figure 3. Experimental validation of the impact size.

Taking into consideration a sharp temperature gradient between the plume and the ambient air, the profile of calculated high-temperature zone was assimilated to the experimentally observable envelope of the plume. The plume size was characterized by the height (H_p) and the radius (R_p) of a cylinder limiting its envelope (Figure 4a). The comparison between experimentally observed plume envelope and the calculated thermal field (Figure 4a) showed a good correspondence for the pulse times << 1 ms, when the plume has a pronounced mushroom shape. However, at bigger times (Figure 4b-c), the calculated height of the plume was increasing more rapidly than experimentally observed (Figure 5a), while the experimentally observed maximal radius of the plume progressively became wider than the calculated one (Figure 5b). The average velocities of vertical plume expansion were estimated to 6.4 m/s for HSI observations and to 7.7 m/s for the model. The H_p/R_p ratio rapidly stabilized at ~3 for the experimentally observed plume and continued to grow continuously up to ~4.5 for the numerical result. The overestimation of plume height by the model can be attributed to the omission of turbulence and other convection phenomena such as the gas flow protecting the welding head lens, the air currents in the welding hall etc.

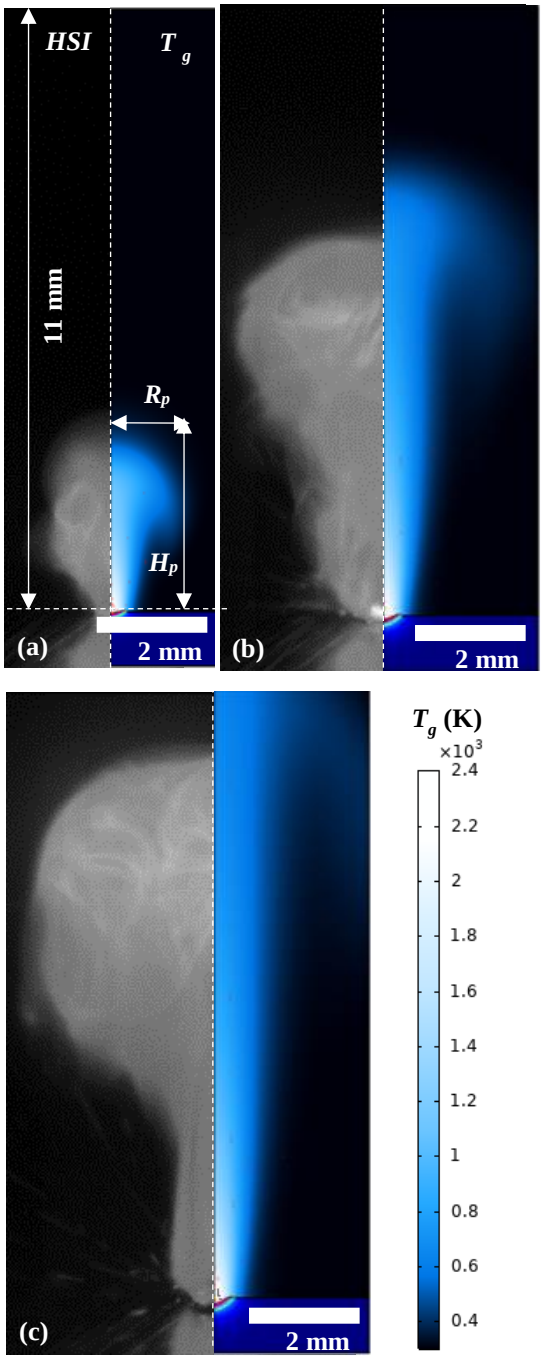

Figure 4. The comparison between the experimentally observed plume (on the left) and the calculated thermal field (on the right) at pulse times of (a) 468 μs, (b) 936 μs and (c) 1404 μs.

5.2. The behavior of the melt and the vapor plume

To represent the global evolution of the melted zone during and after the 2 ms long pulse, the maximal surface temperatures (T_m *max*) and the fraction of liquid metal (f_l) were plotted against time (Figure 6). The first elements of the liquid metal (having f_l = 1) appeared at 25 μs after the start of the pulse, which is reflected by to the sharp increase of surface temperature. In the considered operational conditions, the melt temperature rapidly reaches 2300 K (t = 0.7 ms), which is still below the vaporization temperature of aluminum, and remains constant until the end of the pulse, due to the circular convection in the melt.

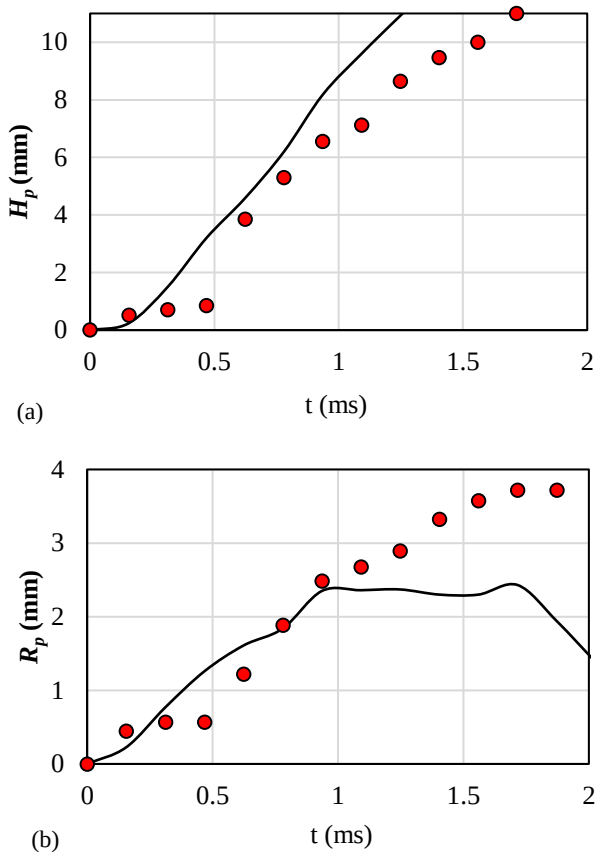

Figure 5. The comparison between the experimentally observed (dots) and calculated dimensions of the plume (line): (a) plume height; (b) maximal plume radius.

The extinction of the laser is followed by a sharp cooling of the metal surface down to 1300 K (t = 2.2 ms). However, the solidification of the melted zone is completed only 1 ms after the extinction of the laser. At 2 ms after the end of the pulse, the metallic domain returns to the ambient temperature. In the chosen operational conditions, some vaporization of aluminum from the melted zone can still take place: the maximal relative pressure (at 2300 K) at the metal/gas interface reached 8700 Pa.

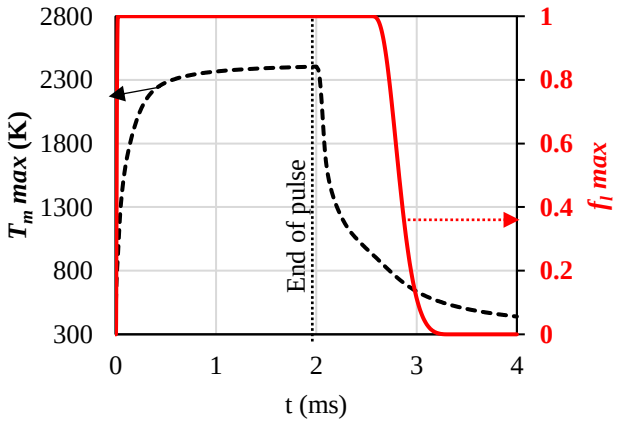

Figure 6. The evolution of maximal temperature and fluid fraction in the melted zone.

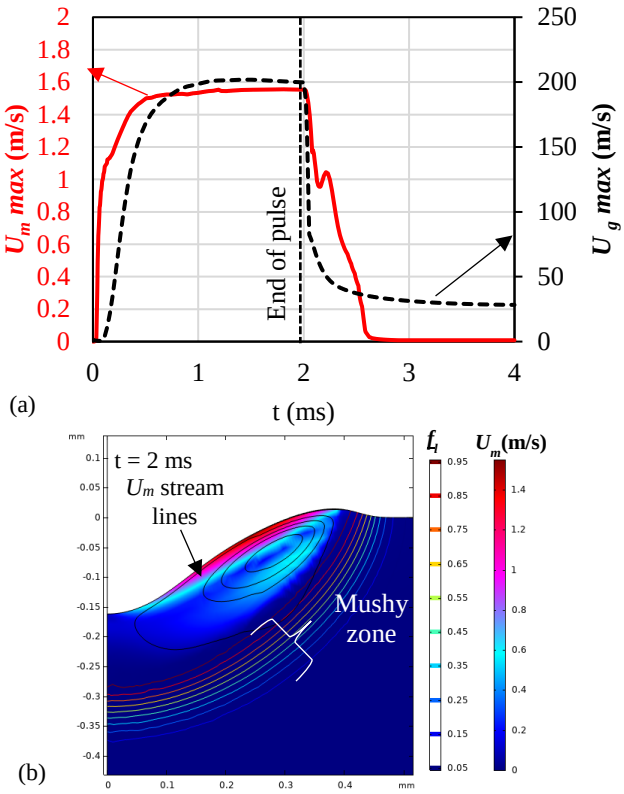

Figure 7. The evolution of maximal velocity field in the melted zone and in the gas phase (a); the velocity field and the fraction of liquid in the melted zone at the end of the pulse (b).

The maximal velocities calculated in liquid and in gas phases were growing up to t = 0.7 ms along with increasing temperature, and then remained constant till the end of the pulse (Figure 7a). The circular convection movements in the melted zone, produced by the recoil pressure and thermocapilary effect, resulted in the maximal velocity of 1.6 m/s in the proximity of the metal/gas surface. At the end of the pulse, the melted zone had an important depression in the center and some liquid matter was displaced toward the borders (Figure 7b). The parasite velocity field in solidified metal was successfully suppressed. The velocity of the gas above the melted zone reached 200 m/s or 0.83 Mach. It is clear that the further increase of laser power (>3 kW) would soon induce the surface temperatures close to the vaporization temperature and produce a supersonic flow of the gas above metal/gas interface, at least for the light metals such as aluminum. After the extinction of the pulse, the velocity of the gas sharply decreased down to the residual values of 25 m/s that correspond to the evacuation of hot air from the cooling metal plate. The maximal velocity field in the metal decreases more progressively, with little fluctuations related to the liquid collapse, and became insignificant 0.5 ms after the end of the pulse.

Besides the lateral vortex, the velocity field of the plume was developing mainly in the vertical direction with a rapid deceleration along z axis (Figure 8). During the pulse, the associated cloud of atoms expanded progressively in a form of a cone. The most concentrated part of the plume was situated next to the metal/gas interface, which justifies the positioning of the spectral acquisition system immediately above the metal surface.

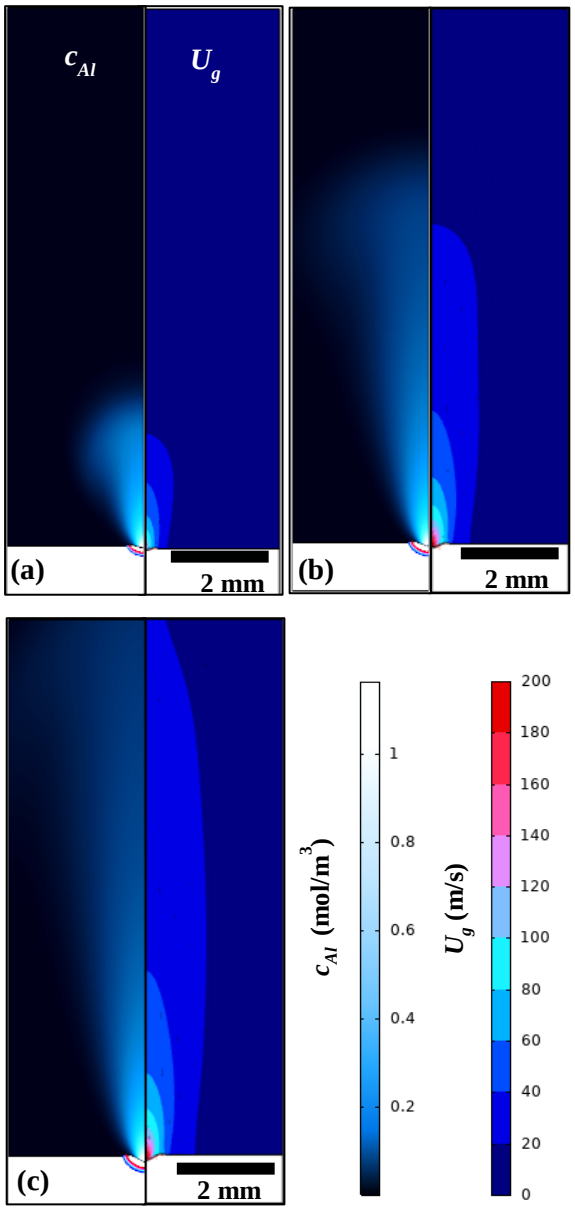

Figure 8. The calculated concentration of Al atoms in the gas phase (on the left) and gas velocity field (on the right) at pulse times of (a) 468 μs, (b) 936 μs and (c) 1404 μs.

The maximal concentration of Al atoms above the metal/gas interface in the considered operational conditions did not exceed 1.5 mol/m^3, which corresponds to ~20% of Al atoms in the most concentrated part of the plume (Figure 9). Such a low molar fraction is determined by the difficulty to bring the aluminum surface to the vaporization temperature, because of its high thermal diffusivity and low absorptivity of laser radiation (considered as 0.15 in this study). Such behavior is consistent with the difficulties to acquire Al emission lines in the similar operational conditions [4]. The rapid dilution of the plume is aggravated by the lower density of Al vapor compared to the density of the surrounding hot air. After the extinction of the laser, the concentration of Al in the gas phase sharply drops below 0.1 mol/m^3 and reaches zero at 0.5 ms after the end of the pulse.

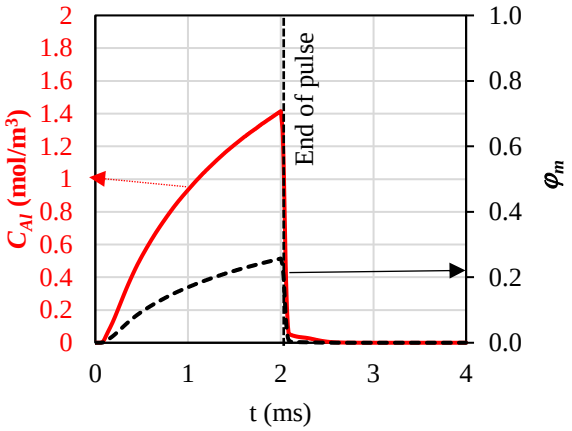

Figure 9. The evolution of maximal Al concentration in the plume (a) and corresponding maximal molar fraction of Al atoms in the air (b).

6. Conclusions

The comparison between calculated thermal field and HSI imaging of the laser-induced plume showed that the proposed multiphysical model allows reproducing the global dynamics of plume propagation during the laser impact on the aluminum alloy surface. The model demonstrated a good correspondence between calculated and experimental dimensions of the impact zone. However, the velocities of plume propagation were overestimated for the times of the pulse > 1 ms, which may be attributed to the existence of turbulent convection and some other possible velocity fields present in the work environment. These effects can be incorporated into the model upon further development.

The maximal gas velocity in the plume neared the sonic speed above the metal/gas interface, but rapidly decreased along the vertical axis. The concentration of Al atoms in the plume was also rapidly decreasing along the vertical axis, which signifies the necessity to target the plume in the immediate proximity of the melt, to increase the chance of obtaining an exploitable emission spectrum. High velocities of the jet produced a sudden drop of Al concentration in the plume after the extinction of the laser.

The present model will be confronted with the results of emission spectroscopy measurements performed in different experimental conditions, to relate the temperature and concentrations of the evaporating species with presence or absence of the chosen excitation lines.

7. References

[1] R. Fabbro, S. Slimani, I. Doudet, F. Coste, F. Briand, Experimental study of the dynamical coupling between the induced vapour plume and the melt pool for Nd–Yag CW laser welding. *Journal of Physics D: Applied Physics*, **39**, 394-400 (2006).

[2] P. Bidare, I. Bitharas, R.M. Ward, M.M. Attallah, A.J. Moore, Fluid and particle dynamics in laser powder bed fusion, *Acta Materialia*, **142**, 107-120 (2018).

[3] C. Aragon, J.A. Aguilera, Characterization of laser induced plasmas by optical emission spectroscopy : A review of experiments and methods. *Spectrochimica Acta B*, **63**, 893-916 (2008).

[4] M. Raja Kumar, J.M. Jouvard, I. Tomashchuk, P. Sallamand, Vapor plume and melted zone behavior during dissimilar laser welding of titanium to aluminum alloy. *Proceedings of the Institution of Mechanical Engineers, Part L: Journal of Materials: Design and Applications*, **234:5**, 681–696 (2020).

[5] T.A. Eppes, I. Milanovic, H. Patrolla, Early Stage Melt Ejection in Percussion Laser Drilling, *Proceedings of Comsol Conference Boston 2012*, October 3-5, 2012, Newton, MA, USA.

[6] S. Sharma, H. Ramkumar, A Pragmatic Multiphysics Numerical Model for Melt Hydrodynamics in Selective Laser Melting, *Proceedings of Comsol Conference Bangalore 2018*, Aug 9-10, 2018, Bangalore, India.

[7] Y. A. Mayi, M. Dal, P. Peyre, M. Bellet, C. Metton, C. Moriconi, R. Fabbro, Two-Phase Flow Modeling of Metal Vaporisation under Static Laser Shot Using a Double ALE Method, *Proceedings of Comsol Conference Lausanne 2018*, October 22-24, 2018, Lausanne, Swissland.

[8] G.M. Arshed, S. Z. Shuja, B.S. Yilbas, M.O. Budair, Numerical investigation of a transient free jet resembling a laser-produced vapor jet. *International Journal of Heat and Mass Transfer*, **47**, 1037-1052 (2004).

[9] C. J. Knight, Theoretical modeling of rapid surface vaporization with back pressure, *American Institute of Aeronautics and Astronautics Journal*, **17:5**, 19–523 (1979).

[10] M. Courtois, M. Carin, P. Le Masson, S. Gaied, M. Balabane. A complete model of keyhole and melt pool dynamics to analyze instabilities and collapse during laser welding. *Journal of Laser Applications*, **26:4**, 042001 (2014).

[11] R. Fabbro, K. Chouf, Dynamical description of the keyhole in deep penetration laser welding, *Journal of Laser Applications*, **12:4**, 142-148 (2000).

[12] E. Guyon, J.P. Hulmin, L. Petit, *Hydrodynamique Physique*, Edition du CNRS (1994).

[13] C. Bonacina, G. Comini, A. Fassano, M. Primicerio, Numerical solutions of phase change problems, *International Journal of Heat Mass Transfer*, **16**, 1825-1832 (1973).

[14] E. N. Fuller, P. D. Schettler, J. C. Giddings, New method for prediction of binary gas-phase diffusion coefficients, *Industrial & Engineering Chemistry*, **58:5**, 18-27 **(**1966).

8. Acknowledgements

This work was supported by the region of Burgundy-Franche-Comté, by French Government and by FEDER, to which we address our sincere thanks.